PAPER

Facile synthesis and enhancement upconversion luminescence of ErF₃ nano/microstructures *via* Li⁺ doping†

Linna Guo, Yuhua Wang,* Zehua Zou, Bing Wang, Xiaoxia Guo, Lili Han and Wei Zeng

A series of ErF₃ samples with different morphologies (flake, truncated octahedral, flower-like and rice-like microcrystals) and sizes (20 nm–2 μm) were prepared by an aqueous-based hydrothermal and coprecipitation route, respectively. The crystal structure of ErF₃ is firstly established *via* the Rietveld refinement result of the powder XRD data. In addition, the ErF₃ matrix without doping sensitizer or activator shows bright red upconversion emission under excitation at 980 nm. It is worthwhile pointing out that ErF₃ with an octahedral morphology demonstrates the highest relative intensity, with that of flower-like microcrystals following, but the nanoflakes show the lowest intensity, and the relative intensity is almost 8 times as low as that of the microcrystals. Further doping with Li⁺ would enhance the upconversion luminescence intensity, and the upconversion emission intensity of the optimal sample with doping 6 mol% Li⁺ is four times stronger than that of a Li⁺ free sample. Furthermore, upon electron beam excitation, the cathodoluminescence properties of a ErF₃ matrix as a new upconversion host are also studied, which is an interesting phenomenon.

1. Introduction

In so-called 'self-activated phosphors' luminescence, *e.g.* under photo excitation, even high quality pure materials can be excited. Such a property is inherent to the ABO₃ perovskite crystal family, which reveals a broad-band emission in the visible spectral region,[1–3] and the donor–acceptor pair recombination, such as W(Nd/Ta)O₄,[4] VO₄.[5] However, there are few reports about the luminescence of the host itself in the form of upconversion (UC).

In particular, studies on UC are mostly limited to fluorides, due to their optical transparency over a wide wavelength range, as well as low phonon cut-off frequency.[6,7] UC emission properties of rare earth (RE) doped trifluoride (YF₃, LuF₃, GdF₃, *etc.*) have been widely studied in recent years,[8–11] but doping would easily lead to lattice impurities, which may increase the multiphonon relaxation rates between the metastable states, thereby reducing the overall visible emission intensity.[12] Therefore, the host itself has upconversion emission properties and could avoid crystal defects and lattice stress. Er³⁺ can act as the optically active center for its partially full 4f electronic configuration. However, as far as we know, there is not any report on the fabrication and optical properties for another trifluoride ErF₃ whether doping sensitizer/activator or not. Therefore, ErF₃, as a

novel UC matrix, which is known to exist in an orthorhombic phase, is taken as a target material to study in this work. Unfortunately, the crystal structure of ErF₃ has not been studied in detail. Considering that the luminescence properties are strongly dependent on the local chemical environment of activator ions, such as coordination number, site symmetry and bond character,[13] so detailed structure information of the ErF₃ is primarily demonstrated in the current study.

From the perspective of application, nano- and micro-materials are needed to be synthesized in large quantities with the desired composition, reproducible size and shape using green, environmentally responsible methodologies.[14] Among them, hydrothermal and coprecipitation methods which use water as the reaction medium have been proven as effective and convenient processes in preparing inorganic materials with diverse controllable morphologies. Herein, a series of ErF₃ samples with different morphologies including nanoparticles, octahedral, flower-like and rice-like microcrystals were obtained by a facile hydrothermal and coprecipitation route, respectively. It is found that the phases and morphologies of the obtained products could be well tuned by changing the pH value of the initial solution, kinds of additives, hydrothermal time and synthetic method. Furthermore, in contrast to green and blue upconversion light, red light can deeply penetrate bio-tissues owing to its longer wavelength (620–750 nm), but only a few studies on brilliant red upconversion luminescence from upconversion nanoparticles were reported.[15] Therefore, the development of upconversion nanoparticles with effective avoidance of short-wavelength emissions and rational tuning of emission peaks

Research Institute of Environmental Materials, Department of Materials Science, Lanzhou University, Lanzhou, China. E-mail: wyh@lzu.edu.cn

This journal is © The Royal Society of Chemistry 2014

J. Mater. Chem. C, 2014, **2**, 2765–2772 | **2765**

into the long-wavelength (red) region are urgently needed. In this paper, we find that ErF_3 matrix without doping any sensitizer or activator shows bright red upconversion emission under excitation at 980 nm, while the green emission intensity is too low to be detected. So ErF_3 host may hold great promise for biological/biomedical applications, considering Li^+ ion has the smallest cationic radius in the periodical table of elements, which is favorable for its movement and site occupation in the host lattice.[16,17] These advantages make it attractive for use in tailoring the local crystal field of the host lattice and enhancing the luminescence intensity. Therefore, this motivated us to design and fabricate Li^+-doped ErF_3 on the basis of the luminescent efficiency and intensity increment. In particular, the integrated UC emission is enhanced *via* Li^+ doping, and the red emission is still dominating the UC spectra. It is also interesting to find that the ErF_3 matrix itself has cathodoluminescence emission under excitation at low electron beam. All in all, the results presented here are not only intriguing for fundamental studies but the ErF_3 host with diverse morphologies would have potential applications in many fields, such as biological/biomedicine, compact solid state lasers, displays, and field emission displays (FEDs), *etc.*

2. Experiment

2.1 Preparation

Synthetic route 1. Rare earth nitrate stock solution was prepared by dissolving the corresponding rare earth oxide in nitric acid at elevated temperature. 10 mL of $Er(NO_3)_3$ (0.1 M) was added into 10 mL of aqueous solution containing trisodium citrate (labelled as Cit^{3-}) with mass equivalent to that of Er_2O_3. After vigorous stirring for 30 min, 6 mmol of NH_4F was added into the above solution. The pH value of the mixed solution was adjusted to about 2 by adding HNO_3 (1 M). After additional agitation for 15 min, the as-obtained mixed solution was transferred into a Teflon bottle held in a stainless steel autoclave, which was sealed and maintained at 180 °C for 48 h. The system was cooled to room-temperature naturally, and the products were collected, purified by ethanol and deionized water several times, and dried at 80 °C for 12 h. The final product ErF_3 was obtained after the corresponding precursors were calcined at 500 °C for 4 h. Besides, sample with other additives, such as PVP, CTAB or $EDTA_2Na$ was prepared by a similar procedure under pH = 2. Sample with no additive was also prepared by a similar procedure but at different pH values (pH = 1, 3, 7 and 10, respectively).

Synthetic route 2. Stock solution of 3.5 mmol NaF in 15 mL aqueous water was injected dropwise into 10 mL of $Er(NO_3)_3$ (0.1 M) solution (pH = 2) at a rate of 1 mL min^{-1}, and the mixture was kept at 75 °C for 2 h under vigorous stirring. Subsequently, the resulting precipitates were collected by centrifugation and washed with water several times. Finally, the products were heated to 400 °C at a rate of 20 °C per minute, and were kept at this temperature for 1 h under N_2 atmosphere. Li^+ doped ErF_3 samples were prepared by the same procedure, except for adding additional relevant $LiNO_3$ into solution of $Er(NO_3)_3$ at the initial stage.

2.2 Characterization

Phase identification was performed *via* XRD analysis (XRD, Model D/MAX-2400 V, Rigaku, Tokyo, Japan) using Cu Kα radiation (1.5405 Å) at 40 kV and 60 mA. The size, shape and structure of the as-prepared samples were characterized by SEM (S-4800). Low- to high resolution transmission electron microscopy (TEM) and selected area electron diffraction (SAED) patterns were recorded using a FEI Tecnai G2 S-Twin with a field emission gun operating at 200 kV. In the measurements of UC emission spectra, a continuous 980 nm laser diode (LD) with maximum power of 1.2 W was used as an excitation source, and the emission was collected using a HORIBA JOBIN YVON Fluorolog-3 Spectrofluorometer system. Low-voltage CL spectra were obtained using a modified Mp-Micro-S instrument.

3. Results and discussion

3.1 Phase and morphology of ErF_3

The composition and phase purity of the products were first examined by XRD. XRD patterns of the samples prepared without additives by hydrothermal treatment at 180 °C for 48 h with various pH values (pH = 1, 3, 7, 10), shown in Fig. 1a. When pH ≤ 3, it is obvious that the locations and relative intensities of the diffraction peaks coincide well with the data reported in the JCPDS standard card (JCPDS no. 30-0056), indicating that pure-phase $(NH_4)_2Er_5F_{17}$ is obtained under these pH conditions. However, when the pH value was adjusted to neutral or alkaline, the diffraction peaks of the resulted product match very well the JCPDS data card 80-2008 except the experimental peaks shift right, which corresponds to the structure of $Er(OH)_{1.57}F_{1.43}$.[17b] In addition, the difference in the relative intensity of crystal diffraction peaks (110) and (101) of $Er(OH)_{1.57}F_{1.43}$ is related to the growth orientation of the crystal. These results indicate that the cubic phase of $(NH_4)_2Er_5F_{17}$ is preferred at low pH values,
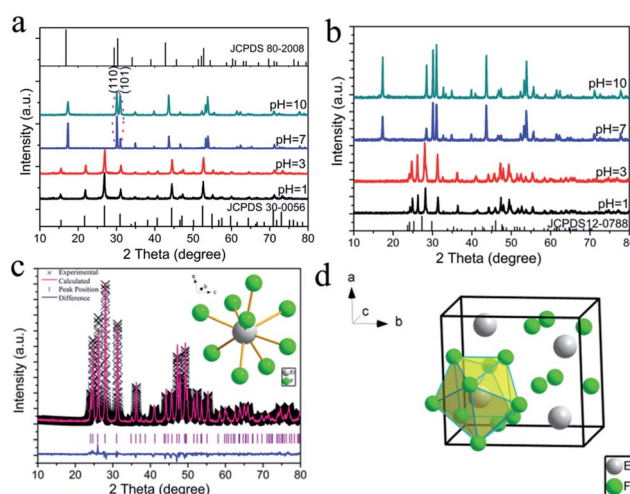

Fig. 1 XRD patterns of precursors (a) and final product after calcination at 500 °C for 4 h (b) with different pH values; Rietveld fitting profiles for ErF_3 host (c); crystal structure of ErF_3 according the Rietveld refinement results (d).

2766 | *J. Mater. Chem. C*, 2014, **2**, 2765–2772

This journal is © The Royal Society of Chemistry 2014

while the hexagonal form of $Er(OH)_{1.57}F_{1.43}$ is more stable at high pH values. Moreover, high crystallinity could be obtained at relatively low synthesis temperature (180 °C), which is important for phosphors, since higher crystallinity always means fewer traps and stronger luminescence.[18] The XRD patterns of these samples described above after heat treatment at 500 °C for 4 h, are also studied, as shown in Fig. 1b. The XRD pattern of samples prepared in acid environment and then after heat treatment at 500 °C for 4 h exhibits prominent peaks in accordance with JCPDS standard card (86-0710) of the ortho-rhombic ErF_3 crystal with no second phase. However, a sample prepared in alkaline environment and then calcinated is not a single phase of ErF_3. On the basis of the XRD patterns of samples prepared at pH = 1 in Fig. 1b, the observed (crosses), calculated (solid line), and difference (bottom)-XRD profiles for the Rietveld refinement of ErF_3 are shown in Fig. 1c. The refined lattice constants of ErF_3 with space group *Pnma* (62) are $a = 6.3038$ Å, $b = 6.8159$ Å, $c = 4.3892$ Å. The reliability parameters of refinement are R_p (%) = 8.5%, R_{wp} (%) = 11.98%, which are within the accepted error range. The crystallographic data and selected bond lengths are summarized in Table 1. According to the Rietveld refinement results, the crystal structure is drawn using Diamond software and shown in Fig. 1d. In the structure of orthorhombic symmetry with space group *Pnma* (no. 62), the Er^{3+} ion lies in the center of an irregular trigonal prism with six fluoride ions at the corners. The three other fluoride ions are symmetrically disposed in front of the prism (see inset of Fig. 1c), therefore the number of fluoride ions around Er^{3+} ions is nine.

Fig. 2 depicts SEM and TEM photographs of the as-prepared precursors described above with different pH values. As can be seen from Fig. 2a, the synthesized particles appear flake-like in shape, and the particles are about 20 nm in thickness and 120 nm in diameter when pH = 1. If the pH value of the initial solution was adjusted to 3, the morphology changed to uniform flowers with an average size of about 395 nm, which is well
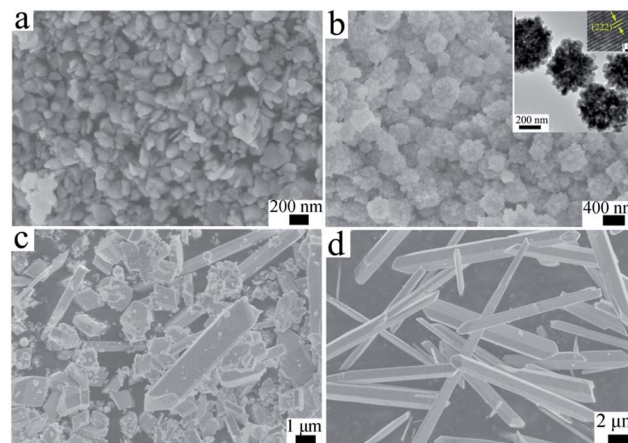

Fig. 2 SEM images of the precursors prepared with different pH values: (a) pH = 1, (b) pH = 3, (c) pH = 7 and (d) pH = 10. TEM and HRTEM images of the precursor prepared with pH = 3 (inset of b).

dispersed (Fig. 2b). To examine the morphology characteristics further, the TEM image is studied, as shown in the inset of Fig. 2b. Nearly mono-disperse and uniform flower-like morphologies with sizes in the range of 385–425 nm are found, and the flower consists of many flakes, consistent with the result of SEM. The obvious lattice fringes confirm the high crystallinity of the sample, and the measured lattice spacing is about 0.32 nm, which could be assigned to the distance of the (222) plane of $(NH_4)_2Er_5F_{17}$ of the cubic phase. If the pH value was further increased to 7 (Fig. 2c), a regular hexagonal prism as a new structure began to emerge, and the rest of the nanoflakes agglomerated seriously. Continuing to increase the pH value to 10, the integral morphology is exactly converted to a uniform hexagonal prism with 12.5 μm in length and 0.85 μm in diameter, and the surface of the hexagonal prism is very smooth (see Fig. 2d). The above results reveal that the final formation phase plays a key role in the shapes and sizes of the as-prepared precursor.

3.1.1 Different additives. Product prepared with PVP, CTAB and Cit^{3-} as chelating agent, respectively, was the standard cubic phase of $(NH_4)_2Er_5F_{17}$ crystal structure, while $EDTA_2Na$ was chosen as chelating agent, the product changed to be an orthorhombic phase of ErF_3 (see the ESI: Fig. S1†). In addition, the corresponding SEM images are illustrated in Fig. 3. When PVP is employed as additive, a large number of uniform 3D flower-like structures of $(NH_4)_2Er_5F_{17}$ with an average diameter of 500 nm were formed, as shown in Fig. 3a. No other morphologies can be observed, indicating a high yield of flower-like microstructures. The TEM image shown in Fig. 3b confirms that the $(NH_4)_2Er_5F_{17}$ flower-like structures are built from nanoflakes, which is in accordance with the SEM image. The obvious contrast shows that void spaces exist in the 3D structures, where the lighter parts correspond to the porosity. The SAED image (Fig. 3c) reveals the flower-like structure consists in strong ring patterns which can be indexed as (222), (400), (600) and (930) planes of cubic $(NH_4)_2Er_5F_{17}$, demonstrating its polycrystalline nature. A representative HRTEM image at the

Table 1 (a) Refinement structure parameters and reliability factor, (b) atom sites parameters

(a)

Formula	ErF₃	
Crystal system	Orthorhombic	
Space group	*Pnma*	
Cell parameters	$a = 6.30382$ Å	$\alpha = \beta = \gamma = 90°$
	$b = 6.81594$ Å	Volume = 180.6 Å³
	$c = 4.38922$ Å	
Reliability factor	$R_{wp} = 11.98\%$	
	$R_p = 8.5\%$	

(b)

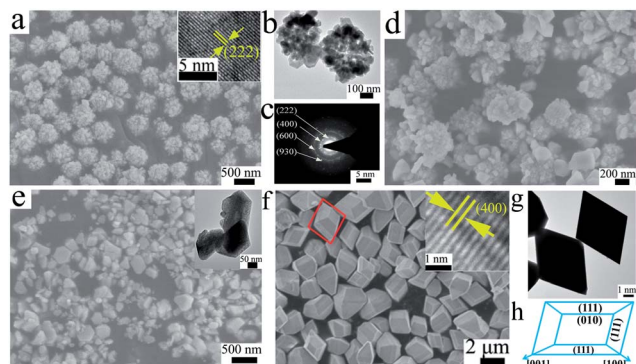| Atom	u	v	w	Occupancy	U_{eq}
F(1)	0.52790	0.25000	0.59596	0.98000	0.00002
F(2)	0.16462	0.06240	0.37190	0.98000	0.00015
Er(1)	0.36750	0.25000	0.05746	0.77686	0.00000

Fig. 3 SEM images of precursors prepared with different additives: (a) PVP, (d) CTAB, (e) Cit^{3-} and (f) $EDTA_2Na$. TEM image (b), HRTEM image (inset of a) and SAED (c) of sample prepared with PVP as additive; TEM image (g) and HRTEM (inset of f) of sample prepared with $EDTA_2Na$ as additive; schematic diagram of the truncated octahedron (h).

edge of an individual $(NH_4)_2Er_5F_{17}$ nanoflake is shown in the inset of Fig. 3a, which further supports the claim of crystallinity for $(NH_4)_2Er_5F_{17}$ microflowers. The lattice fringes are clearly visible with a spacing of 0.31 nm, corresponding to the distance of the (222) plane of $(NH_4)_2Er_5F_{17}$ of the cubic phase. Upon replacing PVP with CTAB while keeping the other parameters unchanged, it can be seen from Fig. 3d that the morphology maintained the flower-like shape, but the size decreased to about 400 nm, and the flower shape became irregular and some fragments also appeared. When Cit^{3-} was used as additive, the morphology changed a great deal, as shown in Fig. 3e. An abundance of almost irregular nanoparticles and nanoflakes with sizes in the range of 130–400 nm can be found. The corresponding TEM image (inset of Fig. 3e) indicated that the obtained samples were irregular nanoflakes. Unexpectedly, when $EDTA_2Na$ was chosen as additive, plenty of almost uniform, regular and truncated octahedra with an average length of about 1.7 μm can be seen in Fig. 3f. It can be seen that the jointed part of the intersecting octahedra, and the imperfections are a result of mismatched closure. Similar results were also observed by Yao *et al.*[19] Well-defined truncated octahedral morphology is characteristic of single-crystalline orthorhombic ErF_3 crystals bound by eight {111} planes (see the red parallelogram of Fig. 3f). The rhombic bases of the truncated octahedron are indexed to the {010} lattice plane. Well-defined nanoparticles with different shapes are observed in the TEM image (Fig. 3g), most are rhombuses, and the others are hexagons. It is known that the hexagons and rhombuses represent, in fact, the same particle morphology observed from different directions. The measured lattice spacing is about 0.16 nm, corresponding to the distance of the {400} plane of the orthorhombic ErF_3 (see the inset of Fig. 3f). Fig. 3h is a schematic diagram of the truncated octahedron.

3.1.2 Different synthetic methods. If the hydrothermal method is changed to be a facile aqueous-based co-precipitation approach under mild conditions (synthetic route 2), the final product is a single phase of ErF_3, so the XRD pattern is not presented here. Interestingly, the morphology changed greatly

to be rice-like shape with a diameter 560 ± 10 nm and length 1250 ± 15 nm, as shown in Fig. 4. The low magnification SEM image (Fig. 4a) shows that microstructures with uniform size were produced at large scale, revealing that the high productivity of the developed method. The products are further examined by TEM (inset of Fig. 4a), which confirmed the uniformity and ellipse geometry of these prepared ErF_3 microcrystals. To reveal the detailed structure of a single ErF_3 particle, selected area electron diffraction (SAED) and high-resolution TEM (HRTEM) analyses were further performed, as presented in Fig. 4b and c. The SAED pattern (Fig. 4b) taken from a single rice-like ErF_3 microcrystal is indexed respectively to the strong concentric rings from the (020), (111), (122), (321), (223) and (351) planes of orthorhombic phase of ErF_3 structure. This observation reveals the polycrystalline nature of the as-prepared rice-like ErF_3 microcrystal. The HRTEM image (Fig. 4c) gave further evidence of polycrystalline behaviour. The spacing between adjacent lattice fringes of ErF_3 microcrystals was 0.322 and 0.356 nm, respectively, which are very close to 0.318 nm for the (111) plane and 0.359 nm for the (101) plane of ErF_3. Fig. 4d shows the EDX spectrum of the obtained product. It can be seen that the major constituents of the as-prepared microcrystals are Er, F and Cu which comes from the copper screen, in agreement with the XRD, SAED, and HRTEM results.

To gain a better understanding of the growth mechanism of the product with flower-like morphology, XRD patterns and morphologies of the product prepared under pH = 3 without any additives are investigated with different hydrothermal times, as shown in Fig. 5. XRD patterns of precursors with different hydrothermal time (Fig. 5a) indicate that if hydrothermal time is shorter than 30 min, the phase of the obtained precursor is a mixed phase of $(NH_4)_2Er_5F_{17}$ and the reaction intermediate, which is marked in Fig. 5a. It is interesting to find that the intensity of XRD peaks of the reaction intermediate is decreased with increasing hydrothermal time, and the phase of the reaction intermediate basically disappears until the hydrothermal time reaches 30 min. The corresponding morphologies (Fig. 5b–d) of precursors prepared with hydrothermal time of 1, 5 or 10 min are consistent with the XRD patterns. From Fig. 5b, when the hydrothermal time is 1 min, the morphology of the precursor is mainly octahedral, but at this time, uneven and incomplete flower-like morphology appeared, and some
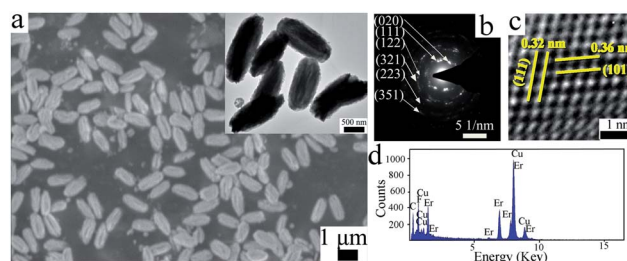

Fig. 4 Low magnification SEM image (a), TEM image (inset of (a)), SAED pattern (b), corresponding high resolution TEM image (c) and EDX spectrum (d) of the obtained product by a a co-precipitation approach.

2768 | *J. Mater. Chem. C*, 2014, **2**, 2765–2772

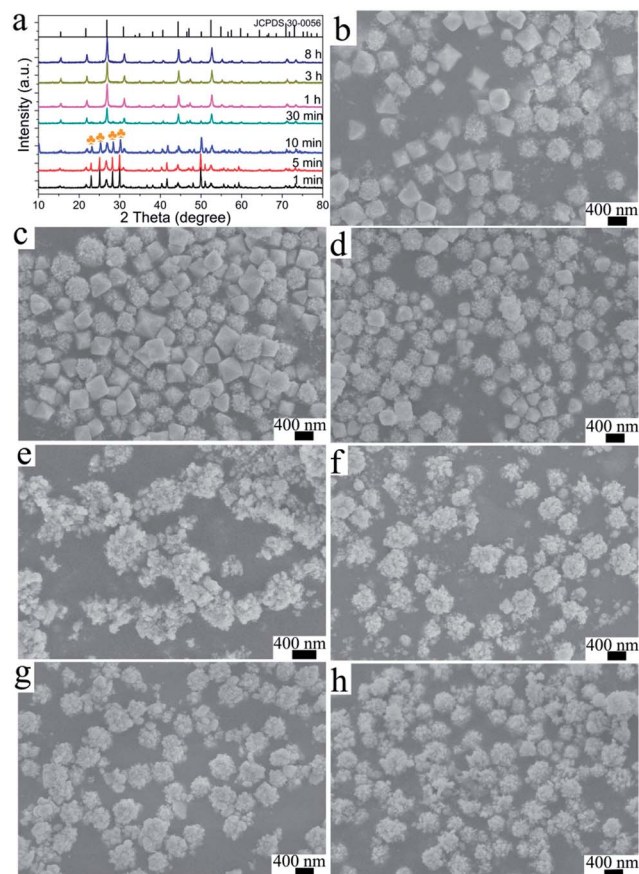This journal is © The Royal Society of Chemistry 2014

Fig. 5 XRD patterns of precursors with different hydrothermal times (a); SEM images of evolution for precursors at different hydrothermal times: 1 min (b), 5 min (c), 10 min (d), 30 min (e), 1 h (f); 3 h (g) and 8 h (h).

nanoparticles in addition to the flower-like material and octahedral microstructures were also observed. Extending the reaction time to 5 min, the flower shape increased more and more with the decrease of the octahedra (Fig. 5c). By contrast, when the reaction time increased to 10 min, it can be seen from Fig. 5d that the flower shape is dominating while the octahedral is in minority. So it is assumed that the octahedral morphology corresponds to the reaction intermediate phase, while the flower morphology indicates the phase of $(NH_4)_2Er_5F_{17}$. In addition, when the hydrothermal time is greater than 30 min, it can be seen from Fig. 5a that the XRD pattern of the precursor is well in agreement with $(NH_4)_2Er_5F_{17}$, and no other phases are found. The corresponding morphologies are shown in Fig. 5e–h, respectively. On the whole, with increasing the hydrothermal time from 30 min to 8 h, the morphology turns irregular and agglomerate flower shape, then regular, uniform and well-dispersed flower but some fragments (nanoparticles) also exist, then it fully developed to 3D-flower shape.

On the basis of time-dependent experiments (SEM in Fig. 5), it can be concluded that ErF_3 microflower-like shape can be obtained *via* a crystallization–dissolution–recrystallization-self-assembly growth mechanism. The nucleation–dissolution–recrystallization growth process was also observed by Qian

et al.[20] and Li *et al.*[21] in the synthesis of t-selenium nanotubes and $BaMoO_4$ nestlike nanostructures. The process of the morphology evolution of ErF_3 flower-like shape is summarized in Scheme 1.

3.2 Luminescence properties

The investigation of upconversion emission light generation starts with a study on ErF_3 itself with different morphologies, as shown in Fig. 6a. It is worth pointing out that ErF_3 itself shows strong red emission and is clearly visible to the naked eye at a pump power density as low as $13.0 \, W \, cm^{-2}$, demonstrating high efficiency of the UC process. No matter what kinds of additives are used, the UC emission is almost red, centered at 661 nm and could be assigned to the intra-4f electronic transitions $^4F_{9/2} \rightarrow {}^4I_{15/2}$ of Er^{3+} ions,[22] while the green emission intensity is too low to detect. To measure the color of the visible emissions of samples with different morphologies that the naked eye perceives, the chromaticity coordinates were calculated from the spectra by the method using the 1931 CIE (Commission Internationale de I'Eclairage France) system. As shown in the inset of Fig. 6a, it can be concluded that the calculated color coordinates shift only slightly and fall within the red region, basically indicating the UC emission has high red color purity. Samples with different morphologies have similar UC emission spectra shapes but different UC emission intensities. The truncated octahedra-like microcrystals prepared using $EDTA_2Na$ demonstrate the highest relative intensity among them, followed by that of flower-like microcrystals used CTAB or PVP as additive, but the nanoparticles prepared using Cit^{3-} show the lowest intensity, and the relative intensity is almost 8 times as low as that of the microcrystals. We ascribe the difference of relative luminescence intensity to different morphologies and sizes of the samples, owing to the fact that morphologies and crystallinity would greatly influence the luminescence properties of inorganic materials.[23] That is to say, products with the same crystal structure with more regular morphology and bigger size would exhibit stronger UC emission. The pump power dependence of red UC emission (inset of Fig. 6a) indicates that it is a "saturated" two-photon absorption mechanism. Fig. 6b shows the dominant UC mechanisms responsible for the emission of red light as well as the schematic representation of the energy levels diagram. The mechanism of the upconverted emission of Er^{3+} has been well established in the literature.[22,24] Accordingly, under excitation with 980 nm light, Er^{3+} ions are excited initially from the ground
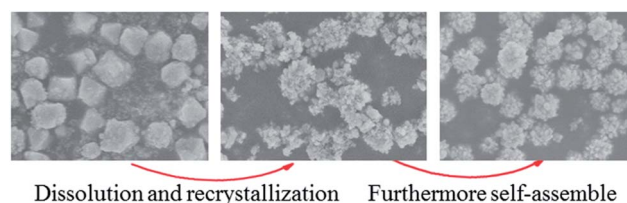
Scheme 1 Schematic illustration of the formation and morphology evolution of ErF_3 flower-like microstructure in the whole synthetic process.
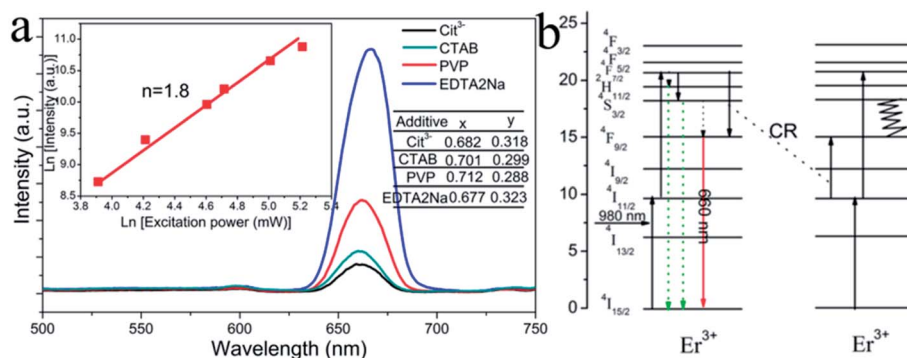
This journal is © The Royal Society of Chemistry 2014

J. Mater. Chem. C, 2014, **2**, 2765–2772 | **2769**

Fig. 6 (a) Upconversion emission spectra of ErF_3 with different morphologies; (b) energy level diagram of the green and red up-conversion emissions from the ErF_3 host by 980 nm LD excitation.

state $^4I_{15/2}$ to the $^4I_{11/2}$ state in the ground-state absorption (GSA) process. Following the excited-state absorption (ESA) process, the Er^{3+} ions are further excited to $^4F_{7/2}$ from the $^4I_{11/2}$ state and subsequently decay to the $^2H_{11/2}$ and $^4S_{3/2}$ states, giving rise to green emission. It is noted that green emission was hardly observed under 980 nm excitation, indicating that the electrons could not be excited to the $^4F_{7/2}$ level. For ErF_3, the concentration of Er^{3+} is high and the Er^{3+} ions have a closer nearest neighbor than others, so a cross-relaxation process is responsible for populating the $^4F_{9/2}$ level and occurs *via* two resonant transitions: $^4F_{7/2} \rightarrow {}^4F_{9/2}$ and $^4I_{11/2} \leftarrow {}^4F_{9/2}$ between neighboring Er^{3+} ions. The $^4F_{9/2} \rightarrow {}^4I_{15/2}$ transition produces red emission around 640–680 nm, giving rise to the domination of red emission.

In order to enhance the UC luminescence intensity, Li^+ ions were introduced into ErF_3 The representative XRD patterns of a series of $ErF_3 : x\%$ Li^+ $(0 \leq x \leq 12)$ samples prepared using the coprecipitation method (synthetic route 2) are shown in Fig. 7a. It is obvious that the location and relative intensity of the diffraction peaks coincide well with the PDF card (JCPDS 86-0710) of ErF_3. No additional peaks of other phases are found, indicating that Li^+ ions have been dissolved successfully in the ErF_3 host. To further investigate the effect of Li^+ ions on the structure of ErF_3, the angles of the main diffraction peak are labeled in Fig. 7b, from which it can be seen that the main diffraction peak of (111) shifts gradually towards larger angles with Li^+ ion doping, indicating Li^+ substituted Er^{3+} according to the effective ionic radii of Er^{3+} and Li^+ are 88.1 and 76.0 pm, respectively. Besides, the changes of the lattice parameter and unit cell volume of the $ErF_3 : x\%$ Li^+ $(0 \leq x \leq 10)$ samples with increased Li^+ concentration are studied, as shown in Table 2. It is clear that both the lattice parameter and unit cell volume decrease with the increased doping concentration of the Li^+ ions, which further indicates that Li^+ ions have been successfully incorporated in the ErF_3 host lattice. As a result, the substitution of Er^{3+} ions can tailor the local crystal field around Er^{3+} ions in the host lattice, which expectedly affects their luminescence.[25] UC emission spectra of a series of ErF_3 samples with various Li^+ concentrations were also investigated, as shown in Fig. 7c. All the obtained emission spectra consist of the f–f transition lines within the Er^{3+} $^4F_{9/2} \rightarrow {}^4I_{15/2}$ (645-680 nm). Upon increasing Li^+

concentration, the peak of the red emission did not shift, while the emission intensity magnified first and then decreased, and the higher incorporation of Li^+ content could not enhance the luminescence anymore, because pairing or aggregation of activator ions at high concentration led to efficient resonant energy transfer between Er^{3+} and Er^{3+} ions and a fraction of energy migration to distant killer or quenchers followed by the appearance of quenching behavior. As can be seen from the inset of Fig. 7c, the color coordinates of $Er_{1-x}Li_xF_3$ $(0 \leq x \leq 12\%)$ were calculated to be in the red region, too.

Interestingly, ErF_3 itself also has cathodoluminescence properties, as shown in Fig. 8a. Under low-voltage electron-beam
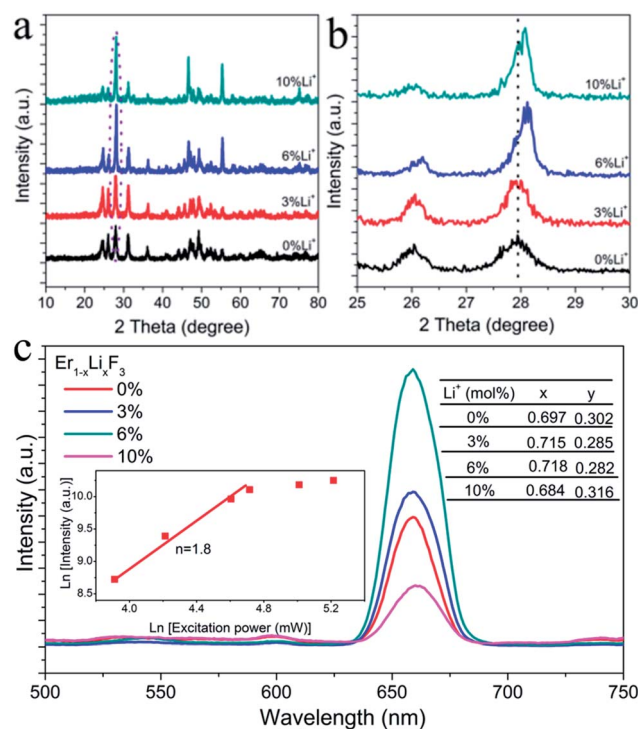

Fig. 7 Powder X-ray diffraction patterns of $Er_{1-x}Li_xF_3$ $(0 \leq x \leq 12\%)$ nanoparticles in range of (a) 10–80°, (b) 28–30°; (c) upconversion luminescence properties of $Er_{1-x}Li_xF_3$ $(0 \leq x \leq 12\%)$.

Table 2 Lattice parameter and unit cell volume of $ErF_3 : x\%$ Li^+ $(0 \leq x \leq 10)$

Samples	Lattice parameters (Å)			Unite cell volume (Å^3)
	a	b	c	
ErF_3	6.320	6.822	4.385	189.1
$ErF_3 : 3\%Li^+$	6.316	6.820	4.382	188.8
$ErF_3 : 6\%Li^+$	6.307	6.819	4.378	188.3
$ErF_3 : 10\%Li^+$	6.299	6.816	4.376	187.9

excitation (accelerating voltage = 8 kV, filament current = 70 mA), the CL spectra of the ErF_3 matrix gave characteristic transitions of Er^{3+} centered at 410 nm ($^2H_{9/2} \rightarrow {}^4I_{15/2}$), 457 nm ($^4F_{5/2} \rightarrow {}^4I_{15/2}$), 506 nm ($^4F_{7/2} \rightarrow {}^4I_{15/2}$), 550 nm ($^4S_{3/2} \rightarrow {}^4I_{15/2}$) and 659 nm ($^4F_{9/2} \rightarrow {}^4I_{15/2}$), respectively.[22] As is well known, the low-voltage CL properties of the materials are important for FEDs, which are promising emissive displays realizing high resolution and low consumption of electric power.[26] So we further investigated the emission properties at various depths from the surface of the ErF_3, as shown in Fig. 8b. The intensity gradually increases as the applied voltage changes from 2 to 10 kV at a current of 90 mA. The increase in CL brightness with an increase in electron energy is attributed to the deeper penetration of electrons into the nanoparticle body and the larger electron-beam current density.[27] Similarly, under a 8.0 kV electron beam excitation, the CL intensity also increases with increasing the filament current from 20 to 100 mA (Fig. 8c). There is no obvious saturation effect for the CL intensity with the increase of the filament current and accelerating voltage, indicating that the ErF_3 matrix is resistant to the current saturation, which is important for FED application.

4. Conclusion

In this work, ErF_3 matrix with different morphologies (flakes, truncated octahedral, flower-like and rice-like microcrystals) and sizes (120 nm–2 μm) were prepared by aqueous-based hydrothermal and co-precipitation route, respectively. It is found that the pH values of the reaction solution, hydrothermal time and kinds of additives have great influence on the phase,

Fig. 8 Cathodoluminescence emission spectra of ErF_3 matrix under accelerating voltage = 8.0 kV, filament current = 80 mA (a); cathodoluminescence intensities of ErF_3 matrix as a function of accelerating voltage (b) and filament current (c).

morphology and size of the product. The crystal structure of ErF_3 is defined to be orthorhombic symmetry with space group *Pnma* (no. 62), and the Er^{3+} ion lies in the center of an irregular trigonal prism. In addition, whatever morphology ErF_3 itself has, ErF_3 shows almost bright red upconversion emission under excitation at 980 nm, owing to the fact that the cross-relaxation process is the main one populating the $^4F_{9/2}$ level of Er^{3+}, and ErF_3 with octahedral morphology has the highest upconversion emission intensity. It is worth noting that upconversion luminescence intensity will be enhanced *via* further doping with Li^+. Furthermore, ErF_3 matrix also has cathodoluminescence properties, which is an interesting phenomenon. As a conclusion, ErF_3 may hold great promise for biological/biomedicine, field emission display devices, *etc*.

Acknowledgements

References

1 R. Leonelli and J. L. Brebner, *Solid State Commun.*, 1985, **54**, 505.

2 H. F. Folkers and G. Blasse, *Chem. Mater.*, 1994, **6**, 969.

3 F. A. Rabuffetti, J. S. Lee and R. L. Brutchey, *Adv. Mater.*, 2012, **24**, 1434.

4 Y. G. Su, C. F. Du, Q. Y. Jia, L. Lv, Q. L. Liu and X. J. Wang, *J. Nanosci. Nanotechnol.*, 2011, **11**, 9855.

5 M. L. Zhao, G. S. Li, J. Zheng, L. P. Li and L. S. Yang, *CrystEngComm*, 2012, **14**, 2062.

6 F. Wang and X. G. Liu, *Chem. Soc. Rev.*, 2009, **38**, 976.

7 P. Y. Qiu, N. Zhou, H. Y. Chen, C. L. Zhang, G. Gao and D. X. Cui, *Nanoscale*, 2013, **5**, 11512.

8 F. Pellé, M. Dhaouadi, L. Michely, P. Aschehoug, A. Toncelli, S. Veronesi and M. Tonelli, *Phys. Chem. Chem. Phys.*, 2011, **13**, 17453–17460.

9 G. F. Wang, W. P. Qin, J. S. Zhang, J. S. Zhang, Y. Wang, C. Y. Cao, L. L. Wang, G. D. Wei, P. F. Zhu and R. Kim, *J. Phys. Chem. C*, 2008, **112**, 12161.

10 C. X. Li, J. Yang, P. P. Yang, H. Z. Lian and J. Lin, *Chem. Mater.*, 2008, **20**, 4317.

11 R. C. Lv, S. L. Gai, Y. L. Dai, N. Niu, F. He and P. P. Yang, *ACS Appl. Mater. Interfaces*, 2013, **5**, 10806.

12 C. H. Henry and D. V. Lang, *Phys. Rev. B: Solid State*, 1977, **15**, 989.

13 J. Wang, M. J. Zhou, S. K. Hark, Q. Li, D. Tang, M. W. Chu and C. H. Chen, *Appl. Phys. Lett.*, 2006, **89**, 221917.

14 (*a*) C. G. Hu, Y. Xi, H. Liu and Z. L. Wang, *J. Mater. Chem.*, 2009, **19**, 858; (*b*) Z. H. Xu, X. J. Kang, C. X. Li, Z. Y. Hou, C. M. Zhang, D. M. Yang, G. G. Li and J. Lin, *Inorg. Chem.*, 2010, **49**, 6706.

15 (*a*) W. Y. Yin, L. N. Zhao, L. J. Zhou, Z. J. Gu, X. X. Liu, G. Tian, S. Jin, L. Yan, W. L. Ren, G. M. Xing and
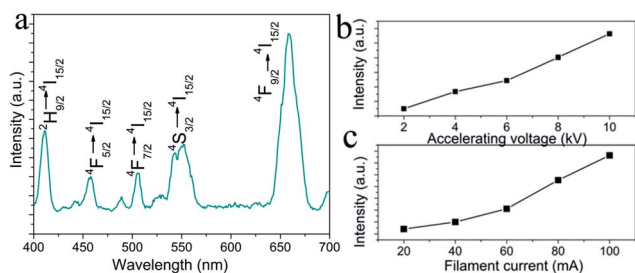
This journal is © The Royal Society of Chemistry 2014

J. Mater. Chem. C, 2014, **2**, 2765–2772 | **2771**

Y. L. Zhao, *Chem. – Eur. J.*, 2012, **18**, 9239; (*b*) J. Zhang, Y. H. Wang, L. N. Guoa and P. Y. Dong, *Dalton Trans.*, 2013, **42**, 3542.

16 Q. Cheng, J. H. Sui and W. Cai, *Nanoscale*, 2012, **4**, 779.

17 (*a*) E. L. Cates, A. P. Wilkinson and J. H. Kim, *J. Phys. Chem. C*, 2012, **116**, 12772; (*b*) L. N. Guo, Y. H. Wang, Y. Z. Wang, J. Zhang, P. Y. Dong and W. Zeng, *Nanoscale*, 2013, **5**, 2491.

18 J. Yang, C. M. Zhang, C. Peng, C. X. Li, L. L. Wang, R. T. Chai and J. Lin, *Chem. – Eur. J.*, 2009, **15**, 4649.

19 F. Tao, Z. J. Wang, L. Z. Yao, W. L. Cai and X. G. Li, *Cryst. Growth Des.*, 2007, **7**, 855.

20 G. C. Xi, K. Xiong, Q. B. Zhao, R. Zhang, H. B. Zhang and Y. T. Qian, *Cryst. Growth Des.*, 2006, **6**, 577.

21 Z. J. Luo, H. M. Li, H. M. Shu, K. Wang, J. X. Xia and Y. S. Yan, *Cryst. Growth Des.*, 2008, **8**, 2275.

22 F. Wang, Y. Han, C. S. Lim, Y. H. Lu, J. Wang, J. Xu, H. Y. Chen, C. Zhang, M. H. Hong and X. G. Liu, *Nature*, 2010, **463**, 1061.

23 T. D. Nguyen, C. T. Dinh and T. O. Do, *ACS Nano*, 2010, **4**, 2263.

24 F. Vetrone, J. C. Boyer, J. A. Capobianco, A. Speghini and M. Bettinelli, *Chem. Mater.*, 2003, **15**, 2737.

25 (*a*) G. Y. Chen, H. C. Liu, H. J. Liang, G. Somesfalean and Z. G. Zhang, *J. Phys. Chem. C*, 2008, **112**, 12030; (*b*) Q. Cheng, J. H. Sui and W. Cai, *Nanoscale*, 2012, **4**, 779.

26 P. Dai, X. Zhang, L. Bian, S. Lu and Y. Liu, *J. Mater. Chem. C*, 2013, **1**, 4570.

27 R. A. Rosenberg, Y. Choi, K. Vijayalakshmi, M. Kareev, J. Tchakhalian, S. Balaz and L. J. Brillson, *Appl. Phys. Lett.*, 2013, **102**, 192910.